Energy & Environmental Science

ROYAL SOCIETY OF CHEMISTRY

PAPER

View Article Online
View Journal | View Issue

Cite this: *Energy Environ. Sci.*, 2025, **18**, 8515

Interfacial supramolecular interactions regulated oligomer networking into robust sub-nanochannels for efficient osmotic energy conversion

Gang Lu, *[a] Hubao A,[b] Hengyue Xu, [c] Yan Zhao, [dk] Yuanyuan Zhao,[e] Huacheng Zhang, [f] Raf Dewil, [dg] Bart Van der Bruggen *[dhi] and Shuang Zheng *[jk]

Oligomer-engineered membranes overcome fundamental limitations in blue energy harvesting by synergistically controlling ion selectivity and flux at the molecular scale. Here, we develop a 5-nm-thick sulfonated membrane fabricated through interfacial supramolecular assembly of tailored oligomers, which addresses key challenges of conventional polymer membranes: the permeability–selectivity trade-off, energy loss in long nanochannels, and inconsistent performance in hypersaline environments. The ultrathin membrane achieves a power density of 10.8 W m^{-2} with 30-day operational stability under a 50-fold NaCl gradient—more than doubling commercial benchmarks (5 W m^{-2}), while maintaining high efficiency (30.7 W m^{-2}) with hypersaline salt-lake brines. This exceptional performance stems from our synergistic design innovations: sub-Debye-length nanoconfinement (0.6 ± 0.2 nm), creating unscreened electric fields for cation-selective transport while excluding anions, programmable chemical heterogeneity enabling surface charge-directed ion transport, and ultrashort pathways (~5 nm) that minimize energy dissipation without compromising selectivity. This work establishes a new framework for nano-confined ion transport, advancing sustainable energy harvesting and redefining the design principles for next-generation separation technologies.

Received 15th June 2025,
Accepted 8th August 2025

DOI: 10.1039/d5ee03350k

rsc.li/ees

Broader context

The global transition to carbon-neutral energy systems urgently requires scalable technologies to harness renewable salinity gradients—a vast but underexploited resource. However, current osmotic energy conversion membranes face an inescapable trade-off: achieving high ion selectivity sacrifices permeability, while boosting permeability compromises stability in real-world hypersaline environments (fundamental limitation). Our work disrupts this paradigm by leveraging supramolecular oligomer networks to create sub-nanometer channels (0.6 ± 0.2 nm) with chemically tailored surfaces. This design simultaneously achieves: (1) record power density (31.3 W m^{-2}, 500× NaCl gradient), outperforming commercial polymer membranes by >300%; (2) unprecedented stability (>25 W m^{-2} for 30 days) in hypersaline solution—addressing the critical scalability gap for coastal/industrial deployment; (3) industrial-process compatibility, demonstrated by roll-to-roll continuous fabrication of large-area membranes. By bridging supramolecular chemistry (molecular-level control) and environmental engineering (real-world brine compatibility), this platform directly supports UN SDG 7 (Affordable Clean Energy) through decentralized blue energy harvesting, water-energy nexus solutions, enabling simultaneous power generation and desalination, and circular economy goals by utilizing hypersaline waste from mining/desalination plants. This work provides both fundamental insights (nanoconfined ion transport under extreme salinity) and a scalable blueprint to unlock osmotic energy—a critical step toward diversifying the renewable energy portfolio.

[a] *Department of Chemical and Biomolecular Engineering, University of Pennsylvania, Philadelphia, PA, 19104, USA. E-mail: ganglu7@seas.upenn.edu*
[b] *State Key Laboratory of Water Resources and Hydropower Engineering Science, Wuhan University, Wuhan, 430072, China*
[c] *Department of Chemistry, Tsinghua University, Beijing, 10084, China*
[d] *Department of Chemical Engineering, KU Leuven, Leuven, Belgium. E-mail: bart.vanderbruggen@kuleuven.be*
[e] *School of Fashion and Textiles, The Hong Kong Polytechnic University, Hong Kong, 999077, China*
[f] *Chemical and Environmental Engineering, School of Engineering, RMIT University, Melbourne, Victoria, 3000, Australia*
[g] *Department of Engineering Science, University of Oxford, Oxford, OX1 3PJ, UK*
[h] *Department of Chemical and Biochemical Engineering, Korea University, 145 Anam-Ro, Sungbuk-Gu, Seoul, 02841, Republic of Korea*
[i] *Nanotechnology Centre, CEET, VSB-Technical University of Ostrava, 17. listopadu 2172/15, Poruba, 708 00, Ostrava, Czechia*
[j] *Kavli Institute for Nanoscience Discovery, Department of Physiology, Anatomy, & Genetics, University of Oxford, Oxford, OX1 3QU, UK. E-mail: shuang.zheng@dpag.ox.ac.uk*
[k] *Department of Civil Engineering, The University of Hong Kong, Hong Kong, 999077, China*

Introduction

The global imperative to achieve carbon neutrality has accelerated demand for renewable energy sources capable of supplementing conventional power generation.[1–5] Among these, osmotic energy, harvested from salinity gradients at seawater-river water interfaces,[6–8] stands out as a scalable and sustainable alternative.[5,9,10] Over the past decades, nanofluidic membranes have emerged as a transformative technology for desalination[3,11–14] and osmotic energy conversion,[8,15–19] leveraging nanoconfinement effects to achieve selective ion transport and high energy conversion efficiency.[20–26] However, despite significant progress, these membranes remain constrained by a fundamental trade-off between permeability and selectivity,[15,16] limiting their practical viability. To address this challenge, recent studies have explored heterogeneous membrane designs incorporating electrostatic, chemical, or structural asymmetries.[27–30] These innovations mitigate concentration polarization and enable directional ion transport, thereby reducing energy dissipation and boosting osmotic energy conversion efficiency.[31–34] Yet, a critical gap persists: balancing high ion throughout with long-term selectivity, particularly in scalable, cost-effective membrane materials.

Polymer-based membranes, prized for flexibility and scalability, represent a promising platform for osmotic energy conversion,[9,35,36] yet their random chain entanglement often limits performance. Here, we exploit the advantage of oligomer—precise structural control, tailored molecular-level interactions, and improved processability—to design an ultrathin sulfonated subnanochannel membrane (SSM). Engineered *via* microphase separation of strategically tailored oligomers confined at air–water interfaces, the SSM addresses the inherent trade-off of permeability and selectivity. The SSM delivers a power density of 31.3 W m^{-2} under a 500-fold NaCl gradient, while sustaining a stable output of >10.8 W m^{-2} over 30 days at a 50-fold gradient. Furthermore, the KCl electrolyte yields the highest power density (13.2 W m^{-2}) under a 50-fold gradient. The outstanding performance arises from its subnanometer-sized channels (<1 nm) coupled with charge heterogeneity across ultrashort pathways (~ 5 nm). These features synergistically enhance ion selectivity and conductivity: the confined subnanoscale channels with gradient sulfonic acid groups create localized electrostatic interactions that amplify cation flux *via* surface charge-directed ions transport. Furthermore, the ultrashort channel length minimizes energy loss, enabling rapid cation transport without sacrificing selectivity. Unlike conventional ultrathin membranes, the SSM's interfacial supramolecular design enables simultaneous control over pore size (sub-Debye-length confinement), surface charge gradient, and mechanical stability, thereby addressing the selectivity–permeability trade-off that limits the use of thicker or disordered membranes. By decoupling ion transport dynamics from traditional polymeric limitations, our work not only advances scalable osmotic energy harvesting but also establishes a new paradigm for designing high-performance ion-selective membranes.

Results and discussion

Preparation of sulfonated tetra-oligomer

Self-assembled oligomers are a versatile tool for designing functional materials due to their structural precision, improved processability, and tunable properties.[13,14,37–41] We herein designed and prepared a sulfonated oligomer, Tetra-PCL-SO_3^-, comprising a four-armed branched polycaprolactone (PCL) with sodium 3-sulfobenzoate end groups (Fig. 1a). The star shape architecture of the tetra-oligomer offers a flexible and processable backbone with mechanical robustness, while its sulfonated groups ensure fast ion transport through the negatively charged subnanochannel membranes. ^{1}H nuclear magnetic resonance (NMR) was used to confirmed the resultant oligomer (Fig. S1). The matrix-assisted laser desorption/ionization time-of-flight (MALDI-TOF) mass spectrum of the tetra-oligomer revealed a major signal of 5142.62 *m*/*z* (Fig. S2), comparable to the theory value. As indicated in Fourier transform infrared (FTIR) analysis (Fig. S3), the new adsorption bands at 1090 and 1238 cm^{-1} are indicative of the asymmetric and symmetric stretching vibration of sulfonate units, and the stretching band at 1168 cm^{-1} corresponds to –O═S═O. X-ray photoelectron spectrum (XPS) further confirm the presence of Tetra-PCL-SO_3^- (Fig. S4), with peaks at 169.7 and 168.5 eV corresponding to S $2p_{1/2}$ and S $2p_{3/2}$ of sulfonate ions, respectively. These characterizations confirmed the successful synthesis of the Tetra-PCL-SO_3^-.

Preparation of sulfonated subnanochannel membranes (SSM)

Chloroform was selected for its ability to dissolve both hydrophobic PCL and hydrophilic sulfonates. Rapid interfacial trapping of oligomers during spreading prevents precipitation, leading to an uniform membrane morphology. The tetra-PCL-SO_3^- oligomer readily dissolves in chloroform, forming a ultrathin membrane when a 5 μL droplet (2 mg mL^{-1}) was spread on a water surface, as indicated in Fig. S5. During interfacial assembly, the hydrophobic PCL chains interact with the water surface, driven by hydrophobic interactions, forming a tightly packed matrix. Simultaneously, the sulfonate-terminated polar groups preferentially oriented toward the aqueous phase, stabilized by hydrogen bonding and electrostatic interactions with water molecules. The fast spreading and evaporation of chloroform at the nanoconfined interface induced rapid solvent displacement, kinetically trapping the oligomers into an ultrathin membrane. This dynamic process leveraged the immiscibility of chloroform and water to achieve two key outcomes: Nanoscale confinement forced the supramolecular alignment of oligomers, creating sub-nanometer channels with charge-dense surfaces; interfacial heterogeneity emerged from competing interactions—hydrophobic PCL aggregation *vs.* hydrophilic sulfonate solvation—yielding a microphase-separated structure resistant to swelling. The rear side, facing to water surface, exhibited a higher negative charge due to increased sulfonation compared to the top side exposed to air (Fig. 1b). Notably, phase separation between the PCL matrix and sulfonic acid groups during droplet spreading on

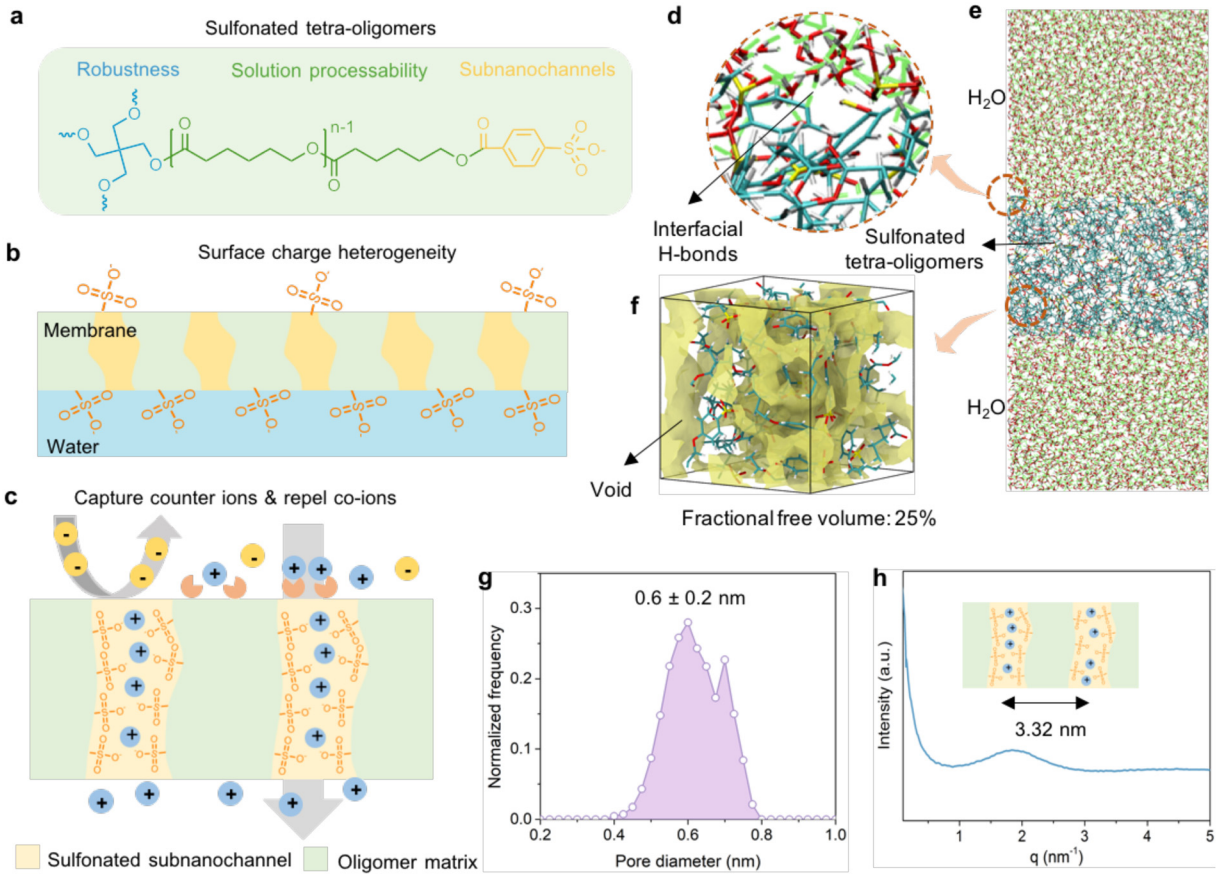

Fig. 1 Sulfonated oligomer-based membranes with subnanochannels coupled with surface charge heterogeneity. (a) The chemical structure of the sulfonated tetra-oligomer. (b) The surface charge heterogeneity enabled by the synergy of interfacial supramolecular interactions under nanoconfinement. (c) Cation-selective subnanochannels that capture counter ions and repel co-ions. (d) The interfacial attractions between sulfonated oligomers and water molecules. (e) The sandwich model composed of sulfonated oligomers and water molecules. (f) The structural model shows the fractional free volume of 25% in the SSM. (g) The pore size distribution determined by a theoretical probe with a radius of 1 Å. (h) The center-to-center distance between adjacent subnanochannels of the SSM analysed by SAXS.

the water interface resulted in the formation of interconnected subnanometer channels enriched with negative charges (Fig. 1c). This unique membrane surface actively captures positive ions while repelling negative ones, and the anionically charged channels facilitate the rapid transport of cations, significantly optimizing ion transfer efficiency.

The formation of subnanochannels in the SSM was investigated (Fig. 1d–g). Molecular dynamics simulations were employed to construct a structural model of Tetra-PCL-SO_3^- on the water surface (Fig. 1e and f), confirming and highlighting interfacial supramolecular interactions such as hydrogen bonding and electrostatic attractions (Fig. 1d). Pore size distributions were calculated, using a theoretical probe with a radius of 0.1 nm, suggesting a narrow pore size range of 0.6 ± 0.2 nm for Tetra-PCL-SO_3^-/H_2O model (Fig. 1g). Small-angle X-ray scattering (SAXS) analysis revealed a shift toward a lower q value upon membrane hydration, indicating a slight expansion of the microphase-separated nanostructure. This behavior originates from the competing effects of hygroscopic sulfonic acid groups attracting water molecules and hydrophobic PCL domains restricting swelling. Quantitative analysis (Fig. 1h and Fig. S6) showed only a minimal increase in the center-to-center distance between adjacent subnanochannels from 3.03 nm (dry state) to 3.32 nm (hydrated state), demonstrating exceptional dimensional stability. The constrained expansion confirms the effectiveness of the PCL network in maintaining structural integrity while preserving the precisely engineered subnanochannels – a critical advantage for stable nanofluidic applications under hydrous conditions.

Characterizations of sulfonated subnanochannel membranes

The ultrathin membranes can be transferred onto diverse substrates for characterizations. The SSM, transferred to a polyethersulfone (PES) membrane, showed high flexibility (Fig. S7). The SSM transferred on a copper grid showed an ultrathin and defect-free surface layer, as indicated in the SEM image (Fig. 2a). The inset image in Fig. 2a depicted a uniform membrane with distinct edges on 300 nm SiO_2/Si wafers, as observed through optical microscopy. GI-XRD profile showed three sharp diffraction peaks that correspond to (110), (111), and (200) planes, indicating a crystalline feature of the SSM (Fig. S8). High-resolution transmission electron microscopy (TEM) further revealed a highly oriented morphology, with

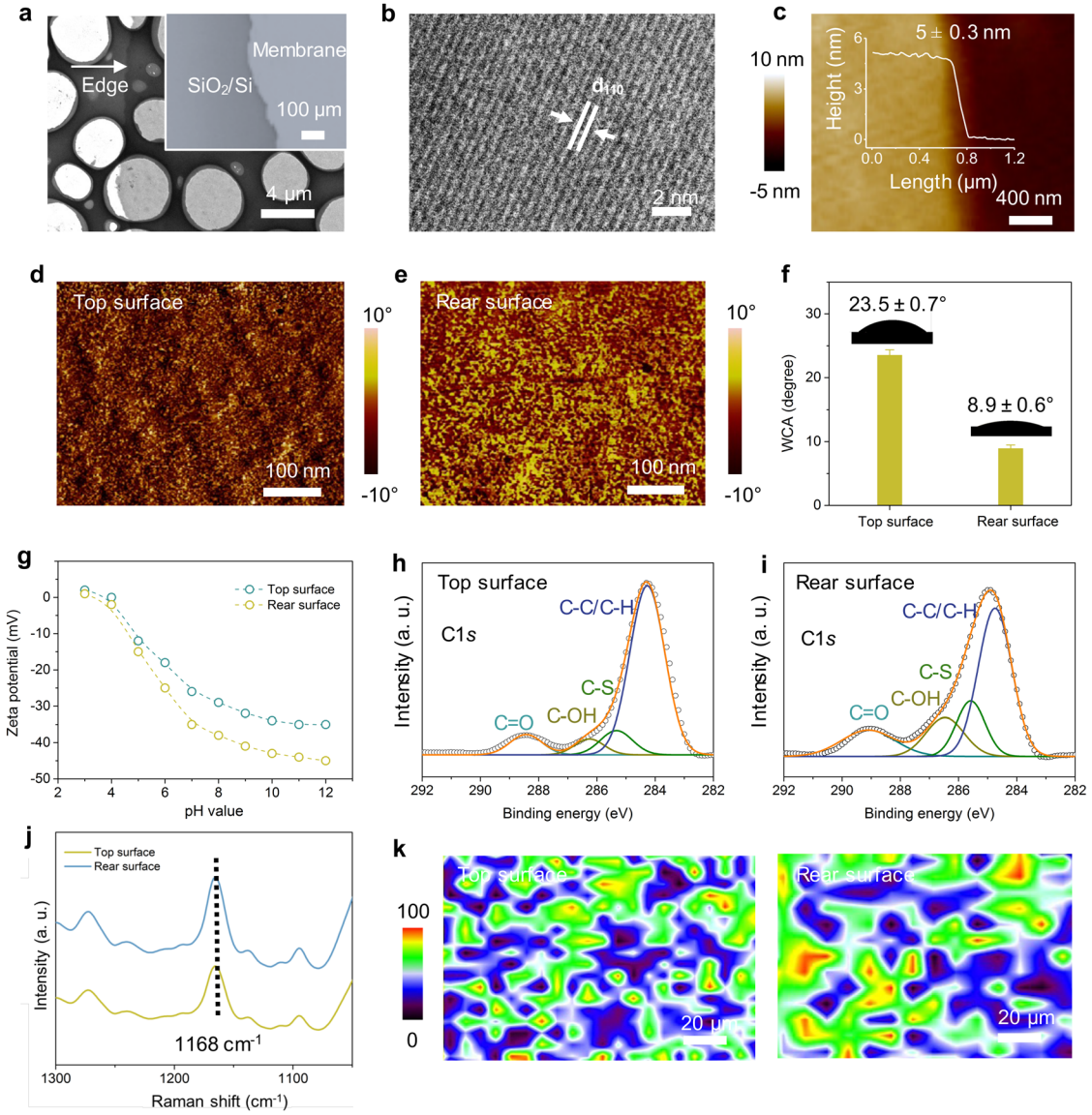

Fig. 2 Characterizations of the SSM. (a) SEM image of the SSM on a copper grid. The inset shows an optical image of the SSM on a SiO_2/Si wafer. (b) The TEM image of the SSM that shows lattice fringes of the (110) plane corresponding to about 0.4 nm. (c) The thickness profile of the SSM on a SiO_2/Si wafer determined by AFM. AFM phase images of the top surface (d) and the rear surface (e) of the SSM. (f) Water contact angles of the top and rear surfaces of the SSM. (g) Zeta potentials of the top and rear surfaces of the SSM. High resolution XPS spectra of carbon element at the top surface (h) and the rear surface (i) of the SSM. Raman spectra (j) and mapping (k) showing the intensity of –O═S═O at 1168 cm^{-1} on top and rear surfaces.

lattice fringes of the (110) plane corresponding to about 0.4 nm (Fig. 2b). Atomic force microscopy (AFM) determined the height profile of the SSM on 300 nm SiO_2/Si wafers to be 5 ± 0.3 nm (Fig. 2c). Besides, the AFM 3D topological measurement (Fig. S9) showed a root mean square roughness (R_q) of 1.37 ± 0.52 nm over a 10 × 10 μm area.

To assess the surface heterogeneity of the SSM, we utilized AFM phase imaging on the top and rear surfaces (Fig. 2d and e). The images revealed a distinct contrast between dark regions, indicative of hydrophobic domains, and bright areas that correspond to hydrophilic domains. This pattern was consistent with the presence of a higher content of sulfonate groups on the rear surface of the SSM. The surface wettability difference is further confirmed by water contact angle measurements. The top side exhibited a contact angle of 23.5 ± 0.7°, while the rear side, with its more distinct hydrophilicity due to increased sulfonation, showed a lower contact angle of 8.9 ± 0.6° (Fig. 2f). The surface charge difference across the pH ranges from 3 to 12 confirmed a higher density of sulfonate ions on the rear side (Fig. 2g). X-ray photoelectron spectroscopy (XPS) analysis revealed the rear surface of the SSM had higher percentages of C–S (13.6%) and C═O (18.4%), and lower intensities of C–C and C–H in C 1s, compared to the top surface (Fig. 2h and i and Table S1). Further, Raman spectra and mapping (Fig. 2j and k) confirmed the higher intensity of –O═S═O at 1168 cm^{-1} on the rear surface, in contrast to the

top surface. These characterizations indicate that nano-confinement-induced interfacial supramolecular attractions lead to notable surface heterogeneities in chemical compositions, surface charges, and wettability.

Efficient osmotic energy harvesting

The ionic transport behaviors of the SSM were characterized by a simple electrochemical setup to measure ionic current (Fig. S10). The 5-nm SSM membrane was secured between two compartments of a test cell. The current–voltage (*I–V*) curve under a symmetric voltage of ±2 V (Fig. 3a) demonstrates a diode-like behavior with a nonlinear *I–V* response recorded in a 0.01 M NaCl electrolyte, indicative of significant ionic rectification. This is attributed to the heterogeneity of surface charge and chemical compositions, leading to asymmetric ionic flow upon the external voltage reversal. The influence of electrolyte concentration on rectification ratios was also studied. As shown in Fig. 3b, rectification ratios peaked at around 50 in a 0.01 M NaCl but decreased with further increases in concentration due to the attenuation of the electrical double layer and the weakening of surface-charge-governed ionic transport. Fig. 3c revealed the dependence of transmembrane ionic conductance on electrolyte concentration. The ionic conductivity follows a linear relationship in high concentrations, while deviating from bulk values at low concentrations, approaching a plateau below 0.1 M, suggesting the surface charge-governed ion transport through the SSM. The stability of ion transport through the SSM was evaluated through a current–time (*I–T*) test in 0.1 M NaCl at pH 7, with an external bias voltage alternating between −1 and +1 V for 5-minute cycles over a total of 60 minutes without break (Fig. S11). The constant currents in both polarities suggest stable ion transport of the SSM.

The SSM, rich in an abundance of surface negative charge, demonstrates a cation-selective potential for salinity gradient power conversion (Fig. 3d). Cations in solution directionally diffused and flowed from high-concentration side to low-concentration side through the ion-selective SSM. The energy conversion behavior was probed through *I–V* curves recorded

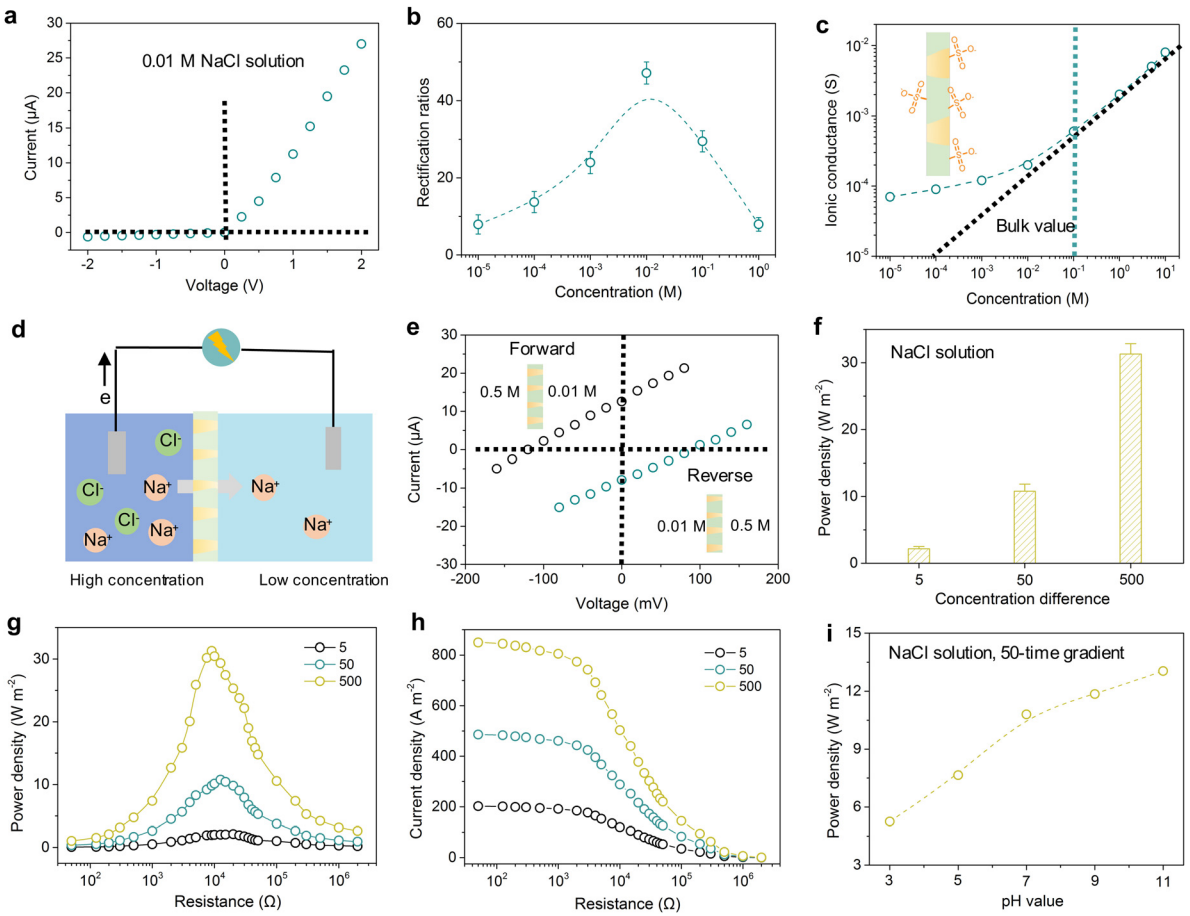

Fig. 3 Transmembrane ionic transport and osmotic energy conversion. (a) The *I–V* curve of the SSM in 10 mM NaCl solutions. (b) Rectification ratios of the SSM as a function of NaCl electrolyte concentration. (c) The effect of the NaCl electrolyte concentration on the ionic conductance. The inset shows the sulfonated groups on the surface of the SSM. (d) Scheme of the energy harvesting process under a concentration gradient. The high concentration is faced to the rear side, and the low concentration is placed on the top side. (e) The forward and reverse configurations for salinity gradient generation under 50-fold concentration gradient. (f) The maximum power density under 5-fold, 50-fold, and 500-fold concentration difference. (g) The power density with the external resistance under 5-fold, 50-fold, and 500-fold concentration difference. (h) The current density with the external resistance under 5-fold, 50-fold, and 500-fold salinity gradient. (i) The maximum power density with pH values from 3 to 11.

under a 0.5 M/0.01 M NaCl concentration gradient (Fig. 3e). Placing the SSM between two-half electrochemical cells with varying NaCl concentrations allowed us to measure open-circuit voltages (V_{OC}) and short-circuit currents (I_{SC}). Under a forward gradient with high concentration on the rear side of the SSM, the absolute V_{OC} and I_{SC} were 125 mV and 12.56 μA, respectively, with an inner resistance ($R_{channel}$) of approximately 9.95 KΩ, calculated by $R_{channel} = V_{OC}/I_{SC}$. In contrast, a reverse 50-fold concentration gradient yielded absolute V_{OC} and I_{SC} of 92.3 mV and 7.6 μA, with inner resistance increasing to 12.14 KΩ. The resistance differences between forward and reverse salinity gradient supports the ionic diode effect, favoring ion transport in the forward gradient direction, thus enhancing energy conversion.

The electric power harvested from the SSM can be utilized to power an electrical load resistor (R_L) in an external circuit. We examined the SSM's energy conversion performance across a range of salinity gradients, as depicted in Fig. 3f–h. The electric power density (P_R) was calculated using the equation $P_R = I^2 \times R_L$. The current density gradually decreased with increasing external resistance, and the output power density reached its peak values when the external load resistance was approximately equal to the SSM's internal resistance. For 5-fold, 50-fold, and 500-fold NaCl salinity gradients, the maximum output power densities reached 2.1, 10.8, and 31.3 W m^{-2}, respectively, at a testing area of 0.03 mm^2. The exceptional power density at a 500-fold concentration gradient showed the SSM's potential in high-salinity applications. Besides, current density increases with the concentration gradient. We noted that the peak powder density at 50-fold NaCl salinity gradient surpassed the commercial benchmark of 5 W m^{-2} under seawater/freshwater conditions.[42–46] The transference number (t_+) denotes a fraction of current carried by cations under a salinity gradient.[17,47] It is calculated by measuring membrane potential in a lab-made two-compartment cell with different solution concentrations. As shown in Fig. S12, at a NaCl solution with 50-fold concentration gradient, t_+ is 0.962 mmol g^{-1}, which confirms exceptional cation selectivity due to sub-Debye confinement (Fig. 1g) and surface charge heterogeneity (Fig. 2g). The SSM achieved an energy conversion efficiency of 42.7% at a 0.5 M/0.01 M NaCl salinity gradient (Fig. S12), attributed to its ultrathin thickness, abundant surface charge, and the ionic diode properties. The power density increased from 5.2 to 13.3 W m^{-2} as pH rose from 3 to 11 (Fig. 3i), highlighting the SSM's superior cation transport rates and selectivity in alkaline conditions, aligning with changes in surface zeta potentials. The SSM demonstrated exceptional long-term stability, maintaining a power density exceeding 10.5 W m^{-2} under a 50-fold salinity gradient for 30 days (Fig. S13). To further evaluate its performance in extreme conditions, we tested the SSM in a hypersaline environment (3 M NaCl *vs.* 0.01 M NaCl) (Fig. S14). Remarkably, the SSM retained a power density of >25 W m^{-2} after 30 days of continuous operation—a record stability for osmotic energy conversion under such aggressive conditions. This unprecedented durability arises from the membrane's microphase-separated architecture, which effectively suppresses swelling and mitigates salt-induced degradation. AFM analysis confirmed the structural integrity of the SSM, with no measurable change in surface roughness after prolonged exposure to 3 M NaCl (Fig. S15), underscoring its robustness in high-salinity scenarios.

High-performance real-world applications

We systematically investigated the effects of membrane thickness, testing area, and electrolyte composition on energy conversion performance. The energy conversion behaviour of the SSM was evaluated using different electrolyte solutions under a 50-fold salinity gradient. As shown in Fig. 4a, the KCl electrolyte yielded the highest power density (13.2 W m^{-2}), with the performance trend across electrolytes following the order: KCl > NaCl > LiCl > $CaCl_2$ > $MgCl_2$. This trend aligns with the observed ion transport behaviour during concentration-driven diffusion (Fig. S15). For these experiments, the feed solution consisted of 0.1 M aqueous solutions of LiCl, NaCl, KCl, $CaCl_2$, or $MgCl_2$, while the permeate side contained deionized water. Inductively coupled plasma optical emission spectrometry (ICP-OES) was used to quantify ion concentrations in the permeate solution. Monovalent ions exhibited higher permeation rates than divalent ions, with the following sequence: $K^+ > Na^+ > Li^+ > Ca^{2+} > Mg^{2+}$ (Fig. S15b). Notably, K^+ achieved the highest permeation rate (0.47 mol m^{-2} h^{-1}) and a remarkable single-salt selectivity of > 50 for K^+/Mg^{2+}, surpassing both Na^+/Mg^{2+} and Li^+/Mg^{2+} selectivities (Fig. S15c) and outperforming reported commercial and reported membranes.[48,49] The superior K^+ transport rate and efficient energy conversion in KCl solution correlate with the density functional theory calculations (Fig. 4b). The binding energy between cations and tetra-PCL-SO_3^- followed a trend of $K^+ < Na^+ < Li^+ < Ca^{2+} < Mg^{2+}$. The inverse relationship between binding energy and permeation rates confirms that stronger cation-membrane interactions generally reduce transport. However, K^+ achieves optimal balance – sufficient binding for exceptional selectivity ($K^+/Mg^{2+} > 50$) while maintaining the highest permeation rate due to its optimal binding strength and the SSM's ultrashort transport paths.

We noted that increased membrane thickness could reduce power density due to higher ion transport resistance (Fig. S16). The 5 nm SSM demonstrated the highest power density, attributed to its high cation flux and low internal resistance. As the testing area increased, the output power density decreased (Fig. S17). This phenomenon aligns with fundamental nanofluidic transport principles elucidated in prior work.[17,49–51] The power density scaling reflects the transition from pore-dominated to entering-resistance-limited transport. Besides, larger membranes introduce additional in-plane resistance (*e.g.*, sheet resistance of the oligomer network) and boundary-layer effects (*e.g.*, salt depletion), further reducing power density. While larger areas face inherent resistance saturation, the SSM's design, such as ultrathin (~5 nm) thickness, defect-free surface, and subnanochannels (~0.6 nm), mitigates these losses, sustaining >5 W m^{-2} even at 25× scaled areas and remarkably surpassing the previous reports.[17,52] Furthermore, we evaluated the SSM's performance

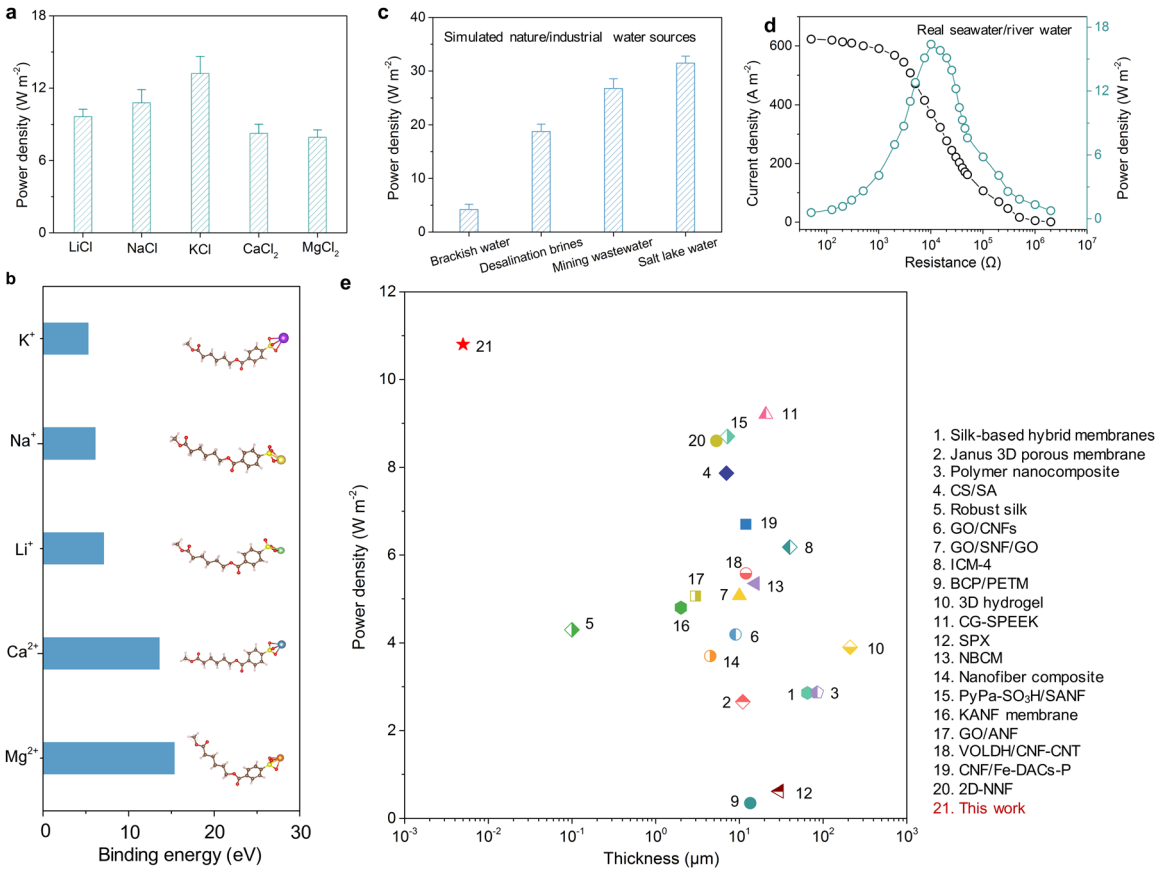

Fig. 4 High-performance real-world applications. (a) The power density under different types of electrolytes. (b) The binding energy of the sulfonated oligomer with different types of electrolytes. (c) The power density under simulated nature and industrial water sources including brackish water, desalination brine, mining wastewater, and salt-lake water. (d) The power density when mixing real seawater from the South China Sea and real river water from the Pearl River. (e) Benchmarking with the reported polymer-based osmotic power generators at the same experimental conditions: a 50-fold NaCl concentration gradient and a testing area of 0.03 mm^2.

with various simulated nature and industrial water sources (Fig. 4c), achieving the maximum power densities of 4.2, 18.8, 26.7, and 30.7 W m^{-2} with brackish water (12 g L^{-1}), desalination brine (75 g L^{-1}), mining wastewater (175 g L^{-1}), and salt-lake water (250 g L^{-1}), respectively. We further assessed the energy harvesting capabilities of the SSM using real seawater from the South China Sea and river water from the Pearl River (Fig. 4d). The SSM achieved an output power density of over 16 W m^{-2} under an approximately 100-fold concentration gradient, which indicates its significant potential for practical applications in hypersaline conditions. In a comparative analysis, we compiled the output power densities of various polymer-based osmotic power generators reported under uniform conditions: a 50-fold NaCl concentration gradient and a testing area of 0.03 mm^2 (Fig. 4e and Table S2). Our SSM demonstrated superior performance, achieving an output power density that markedly exceeds the current state-of-the-art polymer-based osmotic power generators reported in the literature.[31,35,36,42,50,53–66]

Transport mechanism

To explore the mechanisms responsible for the enhanced transmembrane ionic transport and osmotic energy harvesting, a set of systemic molecular dynamics simulations were carried out. The simulation system consists of three parts: an SSM in the middle, with KCl solutions of concentrations 0.5 mol L^{-1} and 0 mol L^{-1} on either side of the membrane (Fig. 5a and b). As shown in Fig. 5c, during the simulation process, K^+ and Cl^- exhibit distinct transport behaviors. K^+ ions preferentially migrate to the membrane surface, subsequently diffuse into the membrane, and ultimately traverse through it. In contrast, Cl^- ions tend to move away from the membrane surface, predominantly residing in regions from it. Such diversity was further quantified by the mean squared displacements and density/number distributions of various components (including membrane, water molecules, K^+, and Cl^-) in the direction perpendicular to the SSM (Fig. 5d–f). More specifically, as illustrated in Fig. 5d, during the initial stage of the simulation (Stage i), K^+ and Cl^- ions are attracted to and repelled by the membrane, respectively, leading to relatively fast movement of both ions and an almost linear increase in MSD_Z (mean squared displacement in the Z-direction). As the simulation proceeds, Cl^- ions, repelled by the membrane, gradually accumulate on the side farther away from the membrane, and their mobility is severely restricted, MSD_Z remains nearly constant. In contrast, K^+ ions are attracted to the membrane and

temporarily adsorb onto it, resulting in a stable MSD_Z (Stage ii). Subsequently, driven by the concentration gradient, K^+ ions detach from the membrane and migrate toward the side with smaller concentration, during which their diffusion ability significantly increases, leading to a rapid rise in MSD_Z (Stage iii). Accompanying the ion transport process, a distinct difference in ion distribution is also observed: K^+ ions preferentially accumulate at the membrane surface, with a small portion also distributed on the opposite side of the membrane (*i.e.*, the lower concentration side), while Cl^- ions gather farther away from the membrane, as shown in Fig. 5e and f.

The distinct transport behaviours of ions are attributed to the presence of $-SO_3^-$ groups, which impart negative charges to the membrane. Therefore, the SSM prefers to attract more positive K^+ ions, and the overall distance between $-SO_3^-$ groups and K^+ ions is smaller than that between $-SO_3^-$ groups and Cl^- ions as shown in Fig. 5g. Additionally, as illustrated in Fig. 5h and i, the interaction properties between the membrane and ions reveal negative interaction energy and force values for K^+ ions, indicating that the membrane tends to attract K^+ ions. Coupled with the inherent pore structure of the membrane, this attraction facilitates the eventual transport of K^+ ions through the membrane. In contrast, the interaction energy and force between the membrane and Cl^- ions are both positive, suggesting that repulsive forces play a dominate role. As a result, Cl^- ions tend to move away from the membrane.

Discussion

This work presents an approach to efficient ion transport and osmotic energy conversion using an ultrathin microphase-separated membrane that features abundant subnanochannels

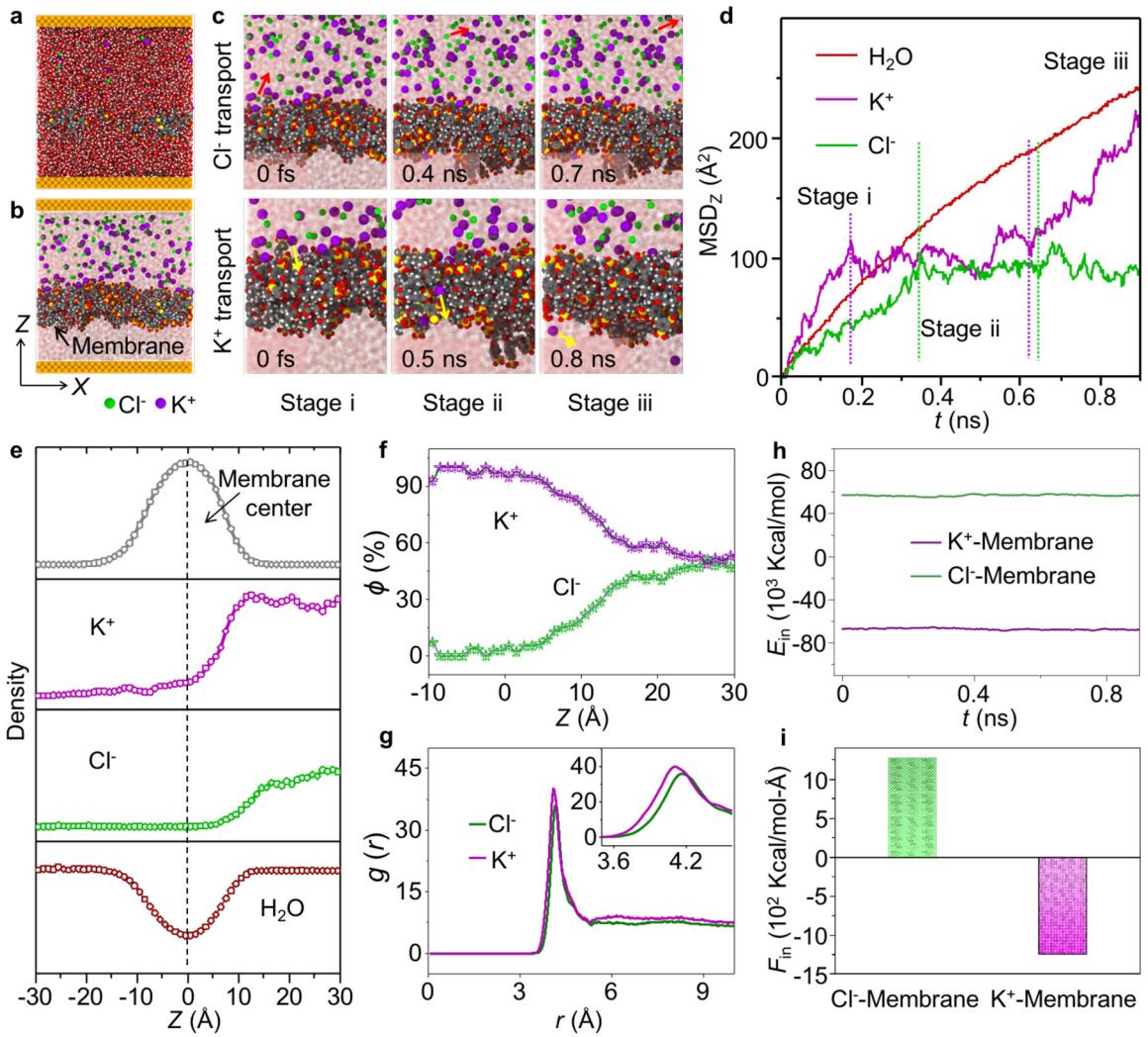

Fig. 5 Transport mechanism. (a) The molecular dynamics simulation system for investigating the transport mechanism of K^+ through the prepared SSM. (b) The water molecules in (a) are set to be semi-transparent for clarity. (c) The distinct transport behaviors and main stages of K^+ and Cl^- during the simulation process. (d) The mean squared displacement of water molecules, K^+, and Cl^- in the direction perpendicular to the SSM (MSD_Z). (e) The density distribution of the SSM, K^+, Cl^-, and water molecules in the direction perpendicular to the SSM. (f) The proportion of K^+ and Cl^- relative to the total number of ions in the direction perpendicular to the SSM. (g) The radial distribution function $g(r)$ between the $-SO_3^-$ groups in SSM and ions. (h) The interaction energy E_{in} between the SSM and ions. (i) The interaction force F_{in} between the SSM and ions.

coupled with surface charge heterogeneity. The interconnected subnanometer channels, enriched with negative charges, enable rapid cation transport, while the membrane's surface heterogeneity, characterized by a higher concentration of sulfonated groups on the rear surface, creates significant variations in charges and wettability between the two sides. The surface charge heterogeneity induces diode-like behaviour with notable ionic rectification, while the cation-selective sub-nanochannels facilitate efficient salinity gradient power conversion, achieving a power density of 10.8 W m^{-2} and an energy conversion efficiency of 42.7% under a 50-fold NaCl solution gradient, surpassing current state-of-the-art polymer-based osmotic power generators. The SSM's real-world applications is demonstrated in both real seawater and river water, showcasing high power densities even under extreme salinity conditions.

Critically, these fundamental breakthroughs are inherently compatible with scalable manufacturing. We demonstrate this through the successful production of 100 cm^2 membranes using roll-to-roll (R2R)-compatible interfacial assembly—a process that combines simplicity with precision (Fig. S20). The approach leverages spontaneous solvent evaporation and supramolecular self-organization, eliminating the need for complex instrumentation while maintaining subnanometer pore uniformity. To bridge the gap between laboratory innovation and industrial adoption, future efforts will prioritize: (1) meter-scale R2R optimization: refining parameters such as spreading kinetics, solvent composition, and environmental controls (humidity/temperature) to enable continuous, high-throughput fabrication; (2) performance amplification at scale: engineering multi-layer SSM architectures to boost power density without increasing footprint, while maintaining mechanical robustness under operational stresses; (3) fundamental advances *via* machine learning: accelerating oligomer design by predicting structure–property relationships (*e.g.*, pore size, charge gradient) to tailor membranes for specific ion selectivities; (4) applications beyond osmotic energy: exploiting the SSM's subnanoconfinement for precision separations (*e.g.*, critical mineral recovery, water purification) and energy storage (*e.g.*, ion-selective battery separators).

This work establishes a transformative paradigm in membrane science, where atomic-scale precision enables macroscopic functional innovation. By uniting mechanistic depth with scalable production, the SSM platform charts a path toward sustainable technologies for energy and resource recovery.

Materials and methods

Materials

ε-Caprolactone (ε-CL), stannous isooctanoate, pentaerythritol, sodium 3-sulfobenzoate, $MgCl_2$ (≥99.99%), $CaCl_2$ (≥97%), KCl (≥99%), NaCl (≥99%), and LiCl (≥99.99%) were purchased from J&K Scientific and used without further purification. Single crystal silicon wafers for atomic force microscopy (AFM) measurement were purchased from Si-Mat Germany.

Methods

Synthesis of tetra-oligomer polycaprolactone (tetra-PCL-OH). Tetra-PCL-OH was synthesized *via* ring-opening polymerization of ε-CL. Pentaerythritol (initiator, 0.1362 g), ε-CL (5 g), and stannous isooctanoate [catalyst, 0.3 wt% (weight %)] were added into a 50-mL flask. The reaction was conducted at 120 °C for 10 hours under argon. The oligomer was dissolved in toluene and precipitated in cold methanol for three times. The product was then vacuum-dried overnight.

Synthesis of tetra-PCL-SO_3Na. Tetra-oligomer PCL (1 mmol) and sodium 3-sulfobenzoate (4 mmol) were added into DMF solution (50 mL). The mixture was vigorously stirred until the solids were fully dissolved. The reaction was then conducted at 120 °C for 5 h under vacuum to facilitate esterification. After the reaction, the oligomer was precipitated in cold ether to remove the unreacted components. The precipitated product was re-dissolved in toluene and reprecipitated in cold ether for three times to ensure purification. The final product was obtained through overnight vacuum drying at 40 °C to remove any residual solvent.

Preparation of sulfonated subnanochannel membranes. The oligomer solution was prepared by dissolving 2 mg of oligomer powder in 1 mL $CHCl_3$. Then, 5 μL of this solution was gently dropped onto the water surface, where it rapidly spread out to form an ultrathin membrane within in a few seconds. This newly formed membrane was then transferred onto appropriate supports for further characterizations.

Characterizations

^1H (400 MHz) NMR spectra were recorded on a Bruker DRX 400 spectrometer using chloroform-d. The molecular weight of the oligomer was determined by MALDI-TOF mass spectrometry using a Bruker model Autoflex TM speed spectrometer. Fourier transform infrared (FT-IR) spectra were captured on a Fourier transform infrared spectrometer (PE Spectrum 100), with wavelengths from 4000 to 400 cm^{-1}. Surface zeta potential of the nano-films was tested by an Anton Paar Surpass solid surface analyzer with 0.01 M KCl solution at ambient temperature over a pH value range of 3–12. The static contact angle and surface tension measurements were conducted with OCA20 equipment from Data Physics, Germany. The crystalline structures were examined by using grazing incidence X-ray diffraction (GIXRD) (Malvern Panalytical's X'Pert3). The membrane was exposed to X-ray for 5 min with an incidence angle of 0.12°. Phase separation was determined by small angle X-ray scattering (SAXS) measurements on SAXSpace. Surface roughness, thickness, and modulus of the nanofilms were measured using atomic force microscopy (AFM; Bruker Dimension Icon with ScanAsyst). The surface roughness is presented as root-mean-square roughness (R_{rms}). The thickness was measured from the distance from the silicon to the nanofilm. The modulus measurements were performed in peak force quantitative nanomechanical mapping (PFQNM) method with the images collected with Si_3N_4 tips (DNP-B, Bruker) at 1.0 Hz scan rate. Chemical element analysis was analyzed by X-ray photoelectron

spectroscopy (XPS; PHI Model 5802). Transmission electronic microscope (TEM; FEI/Philips Tecnai 12 BioTWIN) was used to examine the crystalline structure, with membranes transferred onto copper grids for imaging. The surface morphology was characterized by high resolution scanning electron microscope (SEM; FEI Quanta 450) with an accelerating voltage of 5 kV.

Electrical measurements. The ionic transport properties and the energy conversion efficiency of the SSM were evaluated by measuring the ionic current across the SSM using a Keithley 6487 picoammeter (Keithley Instruments, Cleveland, OH). The membranes were secured between two compartments of a test cell, with an effective membrane area of about 0.03 mm^2. High and low concentration electrolyte solutions were introduced into the respective half-cells, and transmembrane currents were recorded using custom-made Ag/AgCl electrodes. *I–V* curves were obtained under a salinity gradient by applying a scanning voltage ranging from −2 V to +2 V. The open-circuit voltage (V_{OC}) and short-circuit current (I_{SC}) were extracted from *I–V* curves at the intercepts with the voltage and current axes, respectively. The pH values of the electrolytes (KCl or NaCl) solutions were adjusted with acids or bases (HCl/KOH/NaOH), and the electrolyte solutions were refreshed before each measurement to maintain consistency. For practical osmotic energy conversion measurements, the membrane was integrated into an external circuit connected to electrodes within the solution reservoirs to power an electrical load resistor. All electrochemical tests were performed at ambient temperature, with each measurement repeated at least three times to ensure accuracy and reliability of results. For stability testing, the membrane remained clamped in the electrochemical cell throughout the experiment, with the testing solutions being refreshed before each measurement to maintain a consistent concentration gradient.

The cation transfer number (t_+) was calculated by the following equation:

$$t_+ = \frac{1}{2}\left(\frac{E_{\text{diff}}}{\frac{RT}{zF}\ln\frac{\lambda_{C_H}C_H}{\lambda_{C_L}C_L}}\right)$$

where t_+ is the cation transference number, E_{diff} refers to the diffusion potential, R, T, Z, F are the gas constant, temperature, valence charge and Faraday constant, λ and C denote ion activity coefficient and concentration. The subscripts H and L distinguish high and low concentration, respectively.

Energy conversion efficiency is defined as the ratio of the output energy (electrical energy) to the input energy (Gibbs free energy of mixing). The maximum efficiency corresponding to the peak power harvesting, $\eta_{\max}$ is defined as:

$$\eta_{\max} = \frac{(2t_n - 1)^2}{2}$$

where t_n is the cation transference number.

Ion transport performance driven by concentration gradient. The ion separation performance was evaluated under a concentration-driven gradient using a custom diffusion cell apparatus (Fig. S15a). The membrane was mounted between feed and permeate chambers. For single-ion experiments, the feed chamber contained 0.1 M aqueous solutions of KCl, NaCl, LiCl, $CaCl_2$, or $MgCl_2$, while the permeate chamber was filled with deionized (DI) water. Both chambers were continuously stirred with magnetic bars to minimize concentration polarization effects. After each test, the apparatus was rigorously rinsed with DI water to eliminate residual ions, and this process was repeated until the conductivity of the DI water in both chambers matched that of pure DI water. Ion concentrations in the permeate solution were quantified using inductively coupled plasma optical emission spectrometry (ICP-OES).

The ion permeation rate (J_i, mol m^{-2} h^{-1}) calculation is given by:

$$J_i = \frac{(C_1 - C_0)V}{At}$$

where C_0 and C_1 are the initial and current ion molar concentration in the permeate chamber, V is the volume of permeate side solution, A is the effective membrane area (2×10^{-4} m^2), and t is the diffusion time.

The ion selectivity is calculated as follows:

$$S = \frac{J_{i1}}{C_{i1}} \Big/ \frac{J_{i2}}{C_{i2}}$$

where J_i is the permeation rate of ion, and C_i is the concentration of ion in the feed solution.

Density functional theory. In this study, density functional theory (DFT) calculations were performed using the ORCA software package. The molecular geometries were optimized using the B3LYP functional, incorporating Grimme's D3 dispersion correction and the def2-SVP basis set. Tight SCF convergence criteria and the RIJCOSX approximation were applied. All systems take into account the number of charges. The anions carry a negative charge, and the cations are Ca^{2+}, Mg^{2+}, Li^+, Na^+, and K^+.

Molecular dynamics simulations. The chemical structure of a sulfonated tetra-oligomer is shown in Fig. S21a. The classical GROMOS 54A7 force field is employed to describe the interactions between atoms, and the equilibrium molecular structure of the sulfonated tetra-oligomer, shown in Fig. S22b, serves as the basis for subsequent simulations. Additionally, the SPC/E water molecule model is adopted in this work for its balance of computational efficiency and accuracy.

To evaluate the void characteristics of sulfonated subnanochannel membranes on the surfaces of bulk water, sandwich models are constructed, as shown in Fig. S22, with the sulfonated tetra-oligomer layer positioned between two layers of bulk water. The models are then equilibrated under ambient conditions (1 atm and 300 K) until reaching a stable state. Subsequently, an additional 5 ns simulation is performed to collect model configurations for analyzing the void characteristics of the sulfonated tetra-oligomer. Void analysis is conducted using PoreBlazer, with the probe size set to 1.0 Å.

To investigate the mechanisms underlying the enhanced transmembrane ionic transport and osmotic energy harvesting,

a simulation system is constructed as shown in Fig. S23. The system features a sulfonated subnanochannel membrane positioned at the center, flanked by KCl solutions with concentrations of 0.5 and 0 mol L^{-1} on either side. The simulation is carried out for 10 ns until an equilibrium state is reached. During the simulation, key properties of the system, including the density distribution, mean squared displacement, radial distribution function, interaction energy, and interaction force, are analyzed.

All molecular dynamics simulations in this study are conducted under the NPT ensemble at a temperature of 300 K and a pressure of 1 atm, with both temperature and pressure regulated using the Nosé–Hoover method. The velocity-Verlet algorithm, with a time step of 2 fs, is employed to update the positions and velocities of atoms. Periodic boundary conditions are applied in all directions. The simulations are performed using LAMMPS, and the trajectories are visualized with OVITO.

Code availability

The simulation codes used in this study are available from the corresponding authors on request.

Contributions

G. L. conceived the idea, designed and conducted experiments, and drafted the manuscript. G. L. and S. Z. discussed and analysed the results. H. A. performed MD simulations. H. X. conducted DFT simulations. G. L., S. Z., B. V. B., H. Z., R. D. and Y. Z. revised the manuscript. G. L. and H. A. contributed equally. G. L., S. Z., and B. V. B. supervised the study. All coauthors read and commented on the manuscript.

Conflicts of interest

The authors declare no conflict of interest.

Data availability

The data supporting the findings of this study are available within the Article and its SI. Supplementary information available: Figures S1–S23 and Tables S1 and S2. See DOI: **https://doi.org/10.1039/d5ee03350k**

All data are available from the corresponding author upon request.

Acknowledgements

The authors acknowledge the financial support from the RGC General Research Fund (17203924), and the National Natural Science Foundation (22308288). Y. Zhao and B. Van der Bruggen also acknowledge the support provided by the Fonds Wetenschappelijk Onderzoek – Vlaanderen (FWO) (12A6823N and V461824N).

References

1 S. Chu and A. Majumdar, *Nature*, 2012, **488**, 294–303.
2 S. Peng, B. Xie, Y. Wang, M. Wang, X. Chen, X. Ji, C. Zhao, G. Lu, D. Wang and R. Hao, *Proc. Natl. Acad. Sci. U. S. A.*, 2023, **120**, e2303466120.
3 J. Sun, M. U. Farid, W. Xi, G. Lu, M. W. Boey, S. K. Ravi, P. H. L. Sit and A. K. An, *Adv. Funct. Mater.*, 2025, 2416768.
4 J. Yang, B. Tu, G. Zhang, P. Liu, K. Hu, J. Wang, Z. Yan, Z. Huang, M. Fang and J. Hou, *Nat. Nanotechnol.*, 2022, **17**, 622–628.
5 Y. Zhao, J. Liu, G. Lu, J. Zhang, L. Wan, S. Peng, C. Li, Y. Wang, M. Wang and H. He, *Nat. Commun.*, 2024, **15**, 7161.
6 A. Siria, M.-L. Bocquet and L. Bocquet, *Nat. Rev. Chem.*, 2017, **1**, 0091.
7 P. Wang, W. Tao, T. Zhou, J. Wang, C. Zhao, G. Zhou and Y. Yamauchi, *Adv. Mater.*, 2024, **36**, 2404418.
8 M. Rastgar, K. Moradi, C. Burroughs, A. Hemmati, E. Hoek and M. Sadrzadeh, *Chem. Rev.*, 2023, **123**, 10156–10205.
9 Y. Zhao, J. Wang, X.-Y. Kong, W. Xin, T. Zhou, Y. Qian, L. Yang, J. Pang, L. Jiang and L. Wen, *Natl. Sci. Rev.*, 2020, **7**, 1349–1359.
10 S. Zheng, J. Tang, D. Lv, M. Wang, X. Yang, C. Hou, B. Yi, G. Lu, R. Hao and M. Wang, *Adv. Mater.*, 2022, **34**, 2106410.
11 M. Elimelech and W. A. Phillip, *Science*, 2011, **333**, 712–717.
12 G. Lu, Y. Zhao, Y. Zhao, H. Xu, W. Shang, X. Chen, J. Sun, H. Zhang, J. Wu and B. Dai, *Nat. Commun.*, 2025, **16**, 2284.
13 G. Lu, S. Lu, J. Sun, M. W. Boey, W. Shang, J. Wu and A. K. An, *Adv. Funct. Mater.*, 2024, **34**, 2309913.
14 G. Lu, W. Shang, X. Ma, H. Xu, H. A, J. Sun, X. Li, M. Jia, S. Lu and J. Wu, *Nat. Commun.*, 2025, **16**, 6289.
15 W. Xin, L. Jiang and L. Wen, *Acc. Chem. Res.*, 2021, **54**, 4154–4165.
16 X. Tong, S. Liu, J. Crittenden and Y. Chen, *ACS Nano*, 2021, **15**, 5838–5860.
17 L. Ding, M. Zheng, D. Xiao, Z. Zhao, J. Xue, S. Zhang, J. Caro and H. Wang, *Angew. Chem., Int. Ed.*, 2022, **61**, e202206152.
18 W. Jiang, J. Zhou, X. Zhong, M. Fang, J. Hao, D. Zhao, X. Wen, H. Wang, Y. Zhou and Y. Zhu, *Nat. Sustain.*, 2025, **8**, 446–455.
19 Q. Guo, Z. Lai, X. Zuo, W. Xian, S. Wu, L. Zheng, Z. Dai, S. Wang and Q. Sun, *Nat. Commun.*, 2023, **14**, 6702.
20 Z. Zhang, L. Wen and L. Jiang, *Nat. Rev. Mater.*, 2021, **6**, 622–639.
21 W. Guan, R. Fan and M. A. Reed, *Nat. Commun.*, 2011, **2**, 1–8.
22 L. Bocquet and E. Charlaix, *Chem. Soc. Rev.*, 2010, **39**, 1073–1095.
23 K. Xiao, L. Jiang and M. Antonietti, *Joule*, 2019, **3**, 2364–2380.
24 K. Zou, H. Ling, Q. Wang, C. Zhu, Z. Zhang, D. Huang, K. Li, Y. Wu, W. Xin and X.-Y. Kong, *Nat. Commun.*, 2024, **15**, 10231.
25 J. Wang, Z. Song, M. He, Y. Qian, D. Wang, Z. Cui, Y. Feng, S. Li, B. Huang and X. Kong, *Nat. Commun.*, 2024, **15**, 2125.
26 Y. Zhao, X. Yan, L. Xia, Y. Qiu, S. Zheng, G. Lu, Y. Wang, Y. Zhang, J. Shen and X. Zhang, *Sci. Adv.*, 2025, **11**, eadv6646.

27 Z. Zhang, L. Wen and L. Jiang, *Chem. Soc. Rev.*, 2018, **47**, 322–356.
28 L. Ding, D. Xiao, Z. Lu, J. Deng, Y. Wei, J. Caro and H. Wang, *Angew. Chem., Int. Ed.*, 2020, **132**, 8798–8804.
29 Z. Zhang, X. Sui, P. Li, G. Xie, X.-Y. Kong, K. Xiao, L. Gao, L. Wen and L. Jiang, *J. Am. Chem. Soc.*, 2017, **139**, 8905–8914.
30 J. Wang, Z. Cui, S. Li, Z. Song, M. He, D. Huang, Y. Feng, Y. Liu, K. Zhou and X. Wang, *Nat. Commun.*, 2024, **15**, 608.
31 Z. Zhang, L. He, C. Zhu, Y. Qian, L. Wen and L. Jiang, *Nat. Commun.*, 2020, **11**, 875.
32 R. Li, X. Fan, Z. Liu and J. Zhai, *Adv. Mater.*, 2017, **29**, 1702983.
33 W. Guo, Y. Tian and L. Jiang, *Acc. Chem. Res.*, 2013, **46**, 2834–2846.
34 X. Hou, *Adv. Mater.*, 2016, **28**, 7049–7064.
35 W. Chen, T. Dong, Y. Xiang, Y. Qian, X. Zhao, W. Xin, X. Y. Kong, L. Jiang and L. Wen, *Adv. Mater.*, 2022, **34**, 2108410.
36 Q. Zhu, Y. Li, Q. Qian, P. Zuo, M. D. Guiver, Z. Yang and T. Xu, *Energy Environ. Sci.*, 2022, **15**, 4148–4156.
37 M. Liu, P. Liu, G. Lu, Z. Xu and X. Yao, *Angew. Chem., Int. Ed.*, 2018, **130**, 11412–11416.
38 G. Lu, C. Chen, Z. Wang, X. Wu, X. Huang, J. Luo, X.-L. Wang, M.-L. He and X. Yao, *ACS Appl. Mater. Interfaces*, 2023, **15**, 44194–44204.
39 G. Lu, Q. Zhu, R. Ma, W. He and J. Wu, *Adv. Funct. Mater.*, 2023, **33**, 2306914.
40 Y. Zhao, Y. Luo, Y. Chai, Y. Lam, Y. Gong, K. Chen, G. Lu, G. Xia, Y. Chang and M. Yang, *Nano Lett.*, 2025, **25**, 8488–8494.
41 C. Cao, B. Yi, J. Zhang, C. Hou, Z. Wang, G. Lu, X. Huang and X. Yao, *Chem. Eng. J.*, 2020, **392**, 124834.
42 A. Awati, R. Yang, T. Shi, S. Zhou, X. Zhang, H. Zeng, Y. Lv, K. Liang, L. Xie and D. Zhu, *Angew. Chem., Int. Ed.*, 2024, **63**, e202407491.
43 L. Cao, I.-C. Chen, X. Liu, Z. Li, Z. Zhou and Z. Lai, *ACS Nano*, 2022, **16**, 18910–18920.
44 Q. Hou, Y. Dai, X. Zhang and F. Xia, *ACS Nano*, 2024, **18**, 12580–12587.
45 T. Zhu, Y. Kong, B. Lyu, L. Cao, B. Shi, X. Wang, X. Pang, C. Fan, C. Yang and H. Wu, *Nat. Commun.*, 2023, **14**, 5926.
46 J. Gao, W. Guo, D. Feng, H. Wang, D. Zhao and L. Jiang, *J. Am. Chem. Soc.*, 2014, **136**, 12265–12272.
47 P. Zuo, Y. Li, A. Wang, R. Tan, Y. Liu, X. Liang, F. Sheng, G. Tang, L. Ge and L. Wu, *Angew. Chem., Int. Ed.*, 2020, **59**, 9564–9573.
48 T. Xu, B. Wu, W. Li, Y. Li, Y. Zhu, F. Sheng, Q. Li, L. Ge, X. Li and H. Wang, *Sci. Adv.*, 2024, **10**, eadn0944.
49 R. Tan, A. Wang, R. Malpass-Evans, R. Williams, E. W. Zhao, T. Liu, C. Ye, X. Zhou, B. P. Darwich and Z. Fan, *Nat. Mater.*, 2020, **19**, 195–202.
50 Z. Zhang, S. Yang, P. Zhang, J. Zhang, G. Chen and X. Feng, *Nat. Commun.*, 2019, **10**, 2920.
51 J. Gao, X. Liu, Y. Jiang, L. Ding, L. Jiang and W. Guo, *Small*, 2019, **15**, 1804279.
52 C. Chen, D. Liu, L. He, S. Qin, J. Wang, J. M. Razal, N. A. Kotov and W. Lei, *Joule*, 2020, **4**, 247–261.
53 W. Xin, Z. Zhang, X. Huang, Y. Hu, T. Zhou, C. Zhu, X.-Y. Kong, L. Jiang and L. Wen, *Nat. Commun.*, 2019, **10**, 3876.
54 X. Zhu, J. Hao, B. Bao, Y. Zhou, H. Zhang, J. Pang, Z. Jiang and L. Jiang, *Sci. Adv.*, 2018, **4**, eaau1665.
55 R. Li, J. Jiang, Q. Liu, Z. Xie and J. Zhai, *Nano Energy*, 2018, **53**, 643–649.
56 G. Bian, N. Pan, Z. Luan, X. Sui, W. Fan, Y. Xia, K. Sui and L. Jiang, *Angew. Chem., Int. Ed.*, 2021, **133**, 20456–20462.
57 J. Chen, W. Xin, X.-Y. Kong, Y. Qian, X. Zhao, W. Chen, Y. Sun, Y. Wu, L. Jiang and L. Wen, *ACS Energy Lett.*, 2019, **5**, 742–748.
58 Y. Wu, W. Xin, X.-Y. Kong, J. Chen, Y. Qian, Y. Sun, X. Zhao, W. Chen, L. Jiang and L. Wen, *Mater. Horiz.*, 2020, **7**, 2702–2709.
59 W. Xin, H. Xiao, X.-Y. Kong, J. Chen, L. Yang, B. Niu, Y. Qian, Y. Teng, L. Jiang and L. Wen, *ACS Nano*, 2020, **14**, 9701–9710.
60 Z. Zhang, X.-Y. Kong, K. Xiao, Q. Liu, G. Xie, P. Li, J. Ma, Y. Tian, L. Wen and L. Jiang, *J. Am. Chem. Soc.*, 2015, **137**, 14765–14772.
61 Y. Guo, X. Sun, S. Ding, J. Lu, H. Wang, Y. Zhu and L. Jiang, *ACS Nano*, 2024, **18**, 7161–7169.
62 Z. Man, J. Safaei, Z. Zhang, Y. Wang, D. Zhou, P. Li, X. Zhang, L. Jiang and G. Wang, *J. Am. Chem. Soc.*, 2021, **143**, 16206–16216.
63 L. Ding, D. Xiao, Z. Zhao, Y. Wei, J. Xue and H. Wang, *Adv. Sci.*, 2022, **9**, 2202869.
64 J. Chen, W. Xin, W. Chen, X. Zhao, Y. Qian, X.-Y. Kong, L. Jiang and L. Wen, *ACS Cent. Sci.*, 2021, **7**, 1486–1492.
65 Z. Li, D. Wu, Q. Wang, Q. Zhang, P. Xu, F. Liu, S. Xi, D. Ma, Y. Lu and L. Jiang, *Adv. Mater.*, 2024, **36**, 2408364.
66 J. Tang, Y. Wang, H. Yang, Q. Zhang, C. Wang, L. Li, Z. Zheng, Y. Jin, H. Wang and Y. Gu, *Nat. Commun.*, 2024, **15**, 3649.

